International Journal of Energy and Water Resources
https://doi.org/10.1007/s42108-024-00326-8

ORIGINAL ARTICLE

Optimization and numerical simulation of heat sink for cooling electronic chip

A. Singh[1] · **V. Singh**[1] · **V. Trivedi**[1]

Received: 30 July 2024 / Accepted: 16 November 2024

Abstract

In the recent era, electronic equipment like laptops and mobiles have immense popularity among people due to digitalization in every field and sector. The easy handling in fast and busy life requires, the compact shape and light weight of the electronic components. The reduction in the size of the electronic chips enhanced, the energy density per unit volume on the chip material. The increased energy density fails the chips quickly if the produced heat is not removed. In this research article, a heat sink of five rectangular fins has been optimized to maintain the temperature of the microchip of the size 10 mm × 10 mm × 1 mm in the range of 47 °C–50 °C. Initially, the ANSYS 18.1 has been used for determining the chip temperature, pressure drop, and velocity field in the heat sink by using the numerical investigation at varying inlet air velocity, air inlet temperature, and heat generation in the range of 2–4 m/s, 25 °C–35 °C and 1×10^7–2.5×10^7 W/m^3. The data generated by numerical investigation and modeled equations have been optimized using the Response Surface Methodology (RSM). Based on the optimization, the optimum values of the input variables namely air inlet velocity 3.03 m/s, air inlet temperature 25.1010 °C and heat flux 1.12 × 107 W/m3 on which responses Nusselt Number 6.3670, chip temperature 320.0288 K, pressure 2.077 pa, fan power 0.004 W and friction factor 0.1334.

Keywords Heat Sink · Optimization · Numerical analysis · RSM · Nusselt number

Introduction

The higher RAM size and the fast processor enhanced the computer's working speed. It will require fast cooling of the electronic components to avoid heat stroke due to the generation of the higher heat flux (Lin et al., 2005). In 2020, the electronic components were designed up to 100 W/cm^2 but high technical military weapons, laser-guided missiles, and radar technology increase the heat load upto 1000 W/cm^2 (Xie et al., 2013). The above-said problem can be solved by using a heat sink, it will provide the effective cooling of the electronic components by various cooling fluids like air, Nanofluids, Phase Change Material (PCM), and composite fluids (Naqiuddin et al., 2018). The heat sink has been used in every field of engineering like bioengineering, solar panels, fuel cells, and the processor of the computer. The selection of the cooling techniques has been done based on the heat flux generated in the electronic chip. Figure 1 represents the use of cooling techniques based on heat flux supply. For higher heat flux density, forced convection in liquid is desirable since evaporative cooling is much more effective due to latent heat transfer. Table 1 represents the heat transfer coefficient of air and water in free and forced convection.

The heat generated inside the electronic components is carried away by the heat sink through conduction and convection, if the performance of the heat sink is low then a lower amount of heat will flow which causes the failure of the electronic component. However, a number of factors are responsible for the failure of electronic components as shown in Fig. 2. Figure 2 shows that there are four major causes of electronic failure namely dust, humidity, vibration and temperature but 55% of failures in electronic components occur due to temperature. The temperature failure of the electronic components vary exponential with

✉ V. Singh
vineetpsh@gmail.com

A. Singh
anurag.fresher@gmail.com

V. Trivedi
vaibhav.trivedi@iftmuniversity.ac.in

[1] Mechanical Engineering Department, School of Engineering & Technology, IFTM University, Moradabad, India

Published online: 28 November 2024

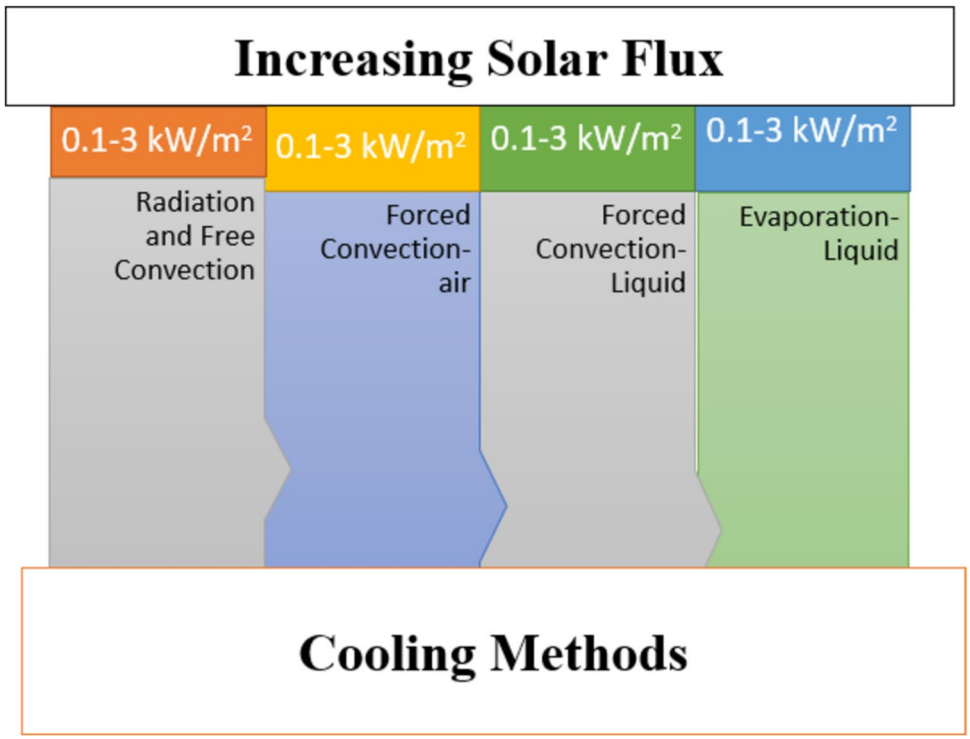

Fig. 1 Cooling methods based on heat flux

Table 1 Heat transfer coefficient of air and water

S. No.	Cooling Modes	Heat Transfer coefficient of air ($W/m^2.k$)	Heat Transfer coefficient of water ($W/m^2.k$)
1	Free Convection	5–100	100–1200
2	Forced Convection (Medium mass flow rate)	10–350	500–3000
3	Boiling	–	3000–100,000

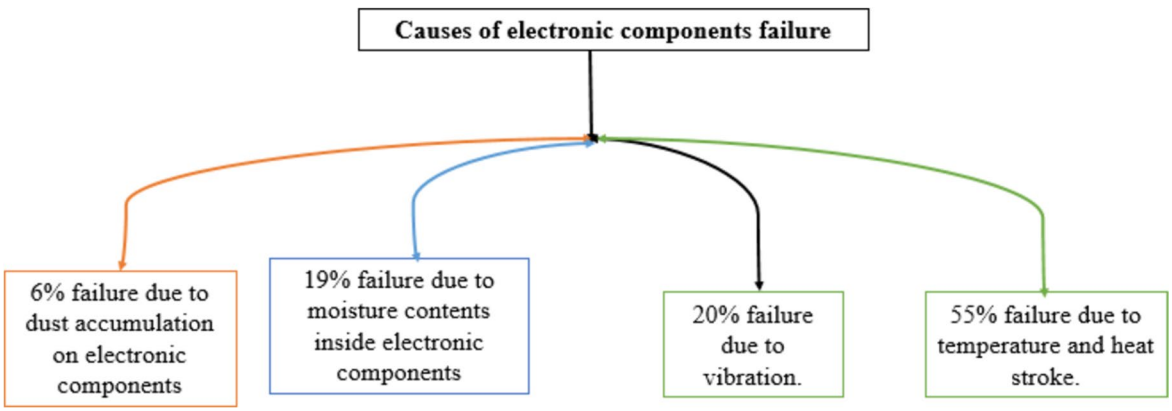

Fig. 2 Causes of the electronic components failure

temperature and represented by following Eq. 1 (Black, 1969; Sohel Murshed & Nieto de Castro, 2017).

$$MTF = \frac{1}{AJ^2}\exp\left(\frac{E_A}{K_B T}\right) \quad (1)$$

The MTF represents, the Median Time of Failure, A is the constant, j is the current density (per/cm^2), E_A is the active energy in (eV), it is around 0.68 eV for the silicon semiconductor, K_B is the Boltzmann Constant and T is the temperature in (K). Sohel Murshed and Nieto de Castro, (2017) represented that after crossing the temperature limit of 75 °C, drastic failure of the electronic components occurs. The author further proved in their findings that at 75 °C, the failure factor is 1 and it reached to be 10 at a temperature of 126 °C. So, heat must be conducted and convected away from the electronic components for safe operation. The performance of the heat sink has been enhanced by either optimizing the geometry or enhance the thermal properties of the heat-carrying fluid. The various geometries of heat sinks adopted in previous research like flat plate (Ahmed, 2016), pin fin (Yang et al., 2019), and the micro-channel for enhancing the performance of the heat sink (Moradikazerouni, et al., 2019). Furthermore, performance has been enhanced by using various types of fluids like air, and water. Nano-fluids (Ranjbarzadeh et al., 2018) (Alsarraf et al., 2019), Phase Change Material (PCM) (Kumar et al., 2023; Zhao et al., 2020).

Among, all fluids air cooling is the best option due to its easy handling, low cost and reliability (Kanargi et al., 2017; Li & Chao, 2009). The main drawback with the air cooling is the low thermal diffusivity due to that its heat transfer capacity is low. As the heat flux increased due to the reduction in the size of the electronic chip water, nano-fluids, Phase Change Material (PCM), and composite fluids are preferred. The water is also mostly used as cooling fluids but it has low thermal conductivity (0.59 W/m.K at 20 °C), the thermal conductivity of the water has been enhanced by mixing the nanoparticles in various concentrations. Along with these cooling fluids three types of the design of the heat sink has been studied in previously published work as presented in Fig. 3. Figure 3 represents the three types of heat sinks namely flat fins, pin fins, and microchannel heat sink.

The heat sink is the main component of the electronic and computing industries for thermal management of the generated heat. The heat sink is generally made by the high thermal conductivity material like the aluminium and copper. The heat sink has been pasted over the heat generated part of the electronic component where generated heat conducted and then convected in the surrounding for maintain the temperature of the electronic component in the desirable limit. The heat sink increases the heat transfer rate by increasing the surface area for that fins are attached at the base of the heat sink. Based on the type of the fins, the heat sink has been classified. In most of the fin-type heat sink air is the cooling fluid which requires less maintenance. The two of the active (Forced Convection) and passive (Free convection) cooling has been used in the heat sink (Singh Yadav et al., 2022; Tejas Sonawane et al., 2016).

First is the flat plate types of heat sinks, these are conventional heat sinks and used for a long time for removing the heat from the confined space. It is used in commuters, space, defense, and solar cells. The air and the water both fluid can be used for transferring the heat but air is more privileged

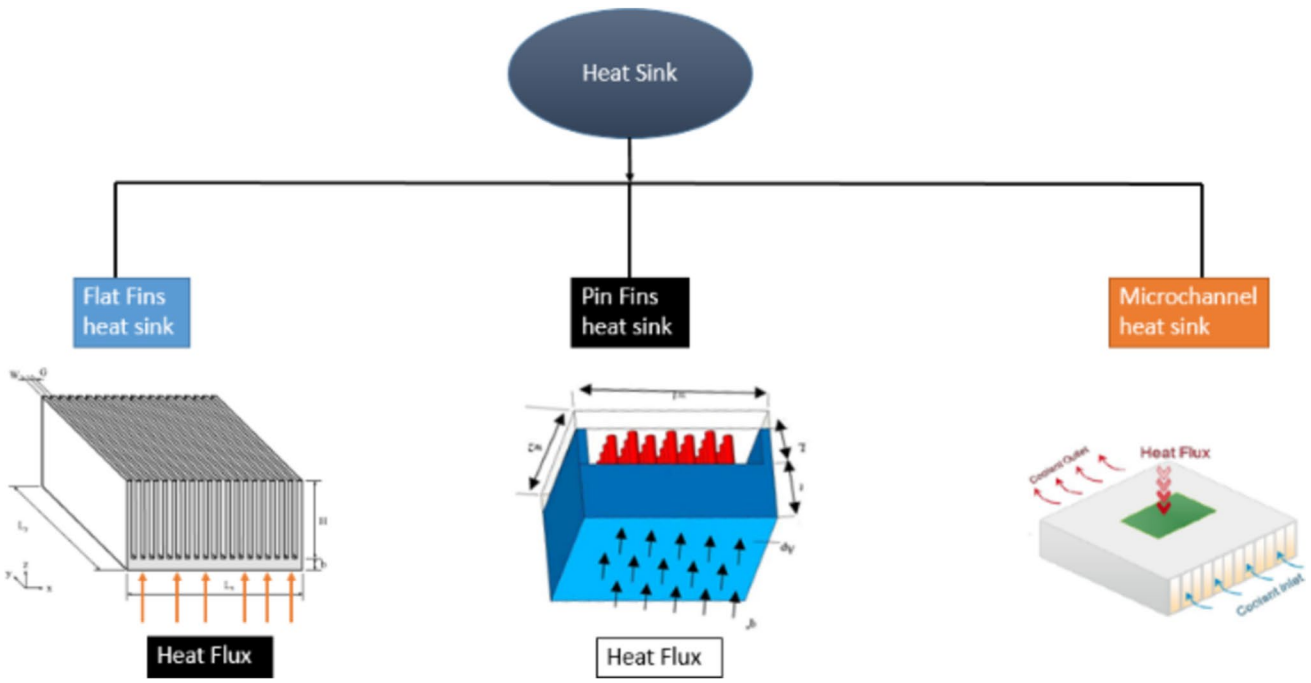

Fig. 3 Various types of heat sink

as compared to water. This type of heat sink is simple, low cost, and easily manufactured. Now at higher solar flux it is obsolete but heat transfer performance is enhanced by creating holes, interruption, and making the surface rough (Singh & Patil, 2015).

Rectangular Flat Plate Heat Sink (RFPHS) is mounted on the slat surface of the heat transfer surface. Figure 6 represents the RFPHS configuration. The configuration of Fig. 6 shows, the flat surface mounted over the rectangular fin. The length of the fin is the same as the flat surface but the height and thickness are different. The selection of the fin height, thickness and pitch done by the optimization methods. The thickness and pitch of the fins are majorly affected the heat transfer characteristics of the heat sink. The number of the previous Numerical and Experimental studies has been published on the flat plate heat sink under the free and forced convection.

The numerical studies are very much effective in the case of heat sink for determining the temperature and pressure through groves provided without spending money in lab experiment. The free and forced convection both types of studies are conducted through the numerical methods. In this section, both studies are discussed one by one.

Tari et al. (2013) investigated, the vertical flat plate heat sink numerically and experimentally at various inclination angles. Their results indicated that at low inclination angles, the convection heat transfer rate remains constant, and slight enhancement is noted at downward inclination. Moreover, the correlation developed by the simulation study have been validated with experimental at wide ranges of the angles namely $-60°$ to $+80°$. Feng et al. (2018) investigated the conventional flat plate heat sink and cross-flow heat sink as presented in Fig. 7. The cross-flow heat sink results have been compared with the conventional heat sink under natural convection conditions. Their results demonstrated that the cross flow heat sink enhanced the overall and convection heat transfer coefficient by 11% and 15% respectively.

Huang et al. (2008) tested the flat fin heat sink in various orientation in natural convection as presenting in Fig. 8. The results demonstrated that downward-face heat sinks have lower heat transfer coefficients and upward and side-way heat sinks have comparable heat transfer coefficients. The heat transfer augmentation for the upward, downward and the sideway heat sink was 1.1–2.5, 0.8–1.8 and 1.2–3.2 respectively. Muneeshwaran et al., (2023) enhanced the performance of the rectangular plate heat sink by doubling the height and spacing of the fin. It augmented the 21% surface area of the heat sink and 17% reduction of the thermal resistance. Their results also indicated the effect of the emissivity on the thermal performance, enhancing the emissivity from 0.15 to 0.9 reduced the thermal resistance by 23%. Luo et al., (2024) conducted a topology optimization on various type of the heat sink design under the CFD analysis. If, the Grashoff Number vary from 2.4×10^2 to 1.2×10^5, the heat transfer rate is enhanced in the range of 37.7% to 49.1%. The primitive design work well at all range of the Grasoff Number due to higher thermal conductivity.

Adhikari et al., (2020) optimized the fins performance in natural convection heat sink. The fin performance has been optimized based on three input variables like height, spacing and length of the fins. The simulation CFD results have been obtained by the Q-Algorithm. Lampio and Karvinen, (2018) developed a model for the reduction time of the CPU calculations. It is made possible by multiobjective optimization for optimizing the geometry of the heat sink. Silva et al., (2019) studied the rectangular heat sink by Open Foam software. The results have been obtained in term of Nusselt Number, temperature, velocity and vorticity field. The open foam results have been validated with the experimental and empirical relation data. Hameed and Khaleel, (2019) numerically investigated the seven different types of the fins. The six wavy shape fins performance has been compared with respect the reference flat fins. The artificial 1000 W heater supply the heat to the heat sink through which 300, 500, and 700 W heat supplied. Results demonstrated that wavy fins with perforation give the best performance. Hooman, (2018) investigated the foam-filled enclosure under theoretical analysis. The scale and thermal resistance analyses both conducted compared and further results validated with literature experimental data. Haghighi et al. (2018) investigated the various types of the flat plate heat sink under natural convection (Fig. 10). The results were determined at various heat input, Rayleigh Number and number of the fins. The heat transfer rate enhanced to be 10–41.6% at 7 fins and spacing 8.5 mm. At, the end the Nusselts Number correlation developed at above said input variables namely the number of fins, fin spacing to height ratio, and Rayleigh Number.

Research gap and aim of the study

The various designs of the heat sink have been investigated in the previous research but air-cooled micro heat sink analyses at various heat generation, inlet air temperature, and inlet air velocity were missing. The main aim of this study is to determine the optimum value of the heat generation, inlet air temperature, and inlet air velocity so that the temperature of the heat sink is lower than 50 °C. The heat sink analyses on microchip of the size 10 mm × 10 mm × 1 mm by numerically and experimentally is novel and new and not found in previous research. This research article also included the optimization by RSM based on the data found through the experimental observations and model equations.

Materials and methods

Methodology for performing the research work

After careful examination of the literature review, it is concluded that the air cooling on the rectangular fins is very cost effective and easy to implement on electronic devices like chip. Put these facts in mind, in this research a microchip of the size 10 mm × 10 mm × 1 mm have been cooled at the various heat generation and flow properties like the inlet air velocity and the heat generation rate. The chip temperature, heat sink, air temperature, velocity, and pressure distribution has been determined by the ANSYS 18.1. Furthermore, the optimum values of the input parameters and responses have been determined by the using Response Surface Methodology (RSM).

Numerical analysis

The numerical analysis of the heat sink has been done in ANSYS 18.1, the fluent tool prefers for the solution of the conservation equations. Fluent uses the finite volume technique to solve the partial differential equation of conservation of mass, momentum, and energy to define the velocity, pressure, and temperature field. Fluent can solve structured and unstructured meshes. Fluent have the capability to solve the variety of the flow problems including the laminar, turbulent, multiphase and chemical mixture. The RNG and k-ε turbulence model has been the approximation used to solve the Navier–stokes equations (Okab et al., 2022; Waila et al., 2022), it is the refined form of the k-ε turbulence model. The RNG k-ε model have the capability to handle rapidly strained fluid flow, it is valid for the high and low Reynolds Number flows. It is assumed that the duct is large enough for the heat sink. So, heat sink and duct both are considered as the isolated system. The duct has a uniform cross-sectional area throughout, which assumed to constant mass flow rate at the inlet and outlet. The wall of the duct is considered as the insulated wall and pressure at the outlet of the duct is the pressure outlet. The heat flux at the base of the heat sink is assumed to be constant and velocity at the inlet of the duct is constant with known magnitude. So, the following are the modified form of the Navier Stokes equations in RNG, k-ε models presented in Kanargi et al. (2018).

Conservation of mass equation presented in Okab et al. (2022).

$$\frac{\partial}{\partial x_i}\left(\rho u_i\right) = 0 \text{ where i } = 1, 2, 3 \tag{2}$$

where ρ is the density of the fluid and u is the velocity of the flow.

Navier–Stokes equation (Maheswari & Prajapati, 2022).

$$\frac{\partial}{\partial x_i}\left(\rho u_i u_j\right) = -\frac{\partial p}{\partial x_i} + \frac{\partial}{\partial x_i}\left[\mu\left(\frac{\partial u_i}{\partial x_j} + \frac{\partial u_j}{\partial x_i}\right) - \overline{\rho u_i u_j}\right] \tag{3}$$

where P is the pressure and μ is the dynamic viscosity.

Energy equation (Maheswari & Prajapati, 2022)

$$\frac{\partial}{\partial x_j}\left(\rho T u_j\right) = \frac{\partial}{\partial x_j}\left[(\mu/Pr)\frac{\partial T}{\partial x_j} - \overline{\rho T' u_j'}\right] \tag{4}$$

where T is the temperature of the fluid and Pr is the Prandlt number.

$$\frac{\partial}{\partial x_j}\left(\frac{k\partial T}{\partial x_j}\right) = 0 \tag{5}$$

where k is the turbulent kinetic energy.

The turbulent stress is represented by following equation (Bondareva & Sheremet, 2022).

$$-\overline{\rho u_i u_j} = \mu_t\left(\frac{\partial u_i}{\partial x_j} + \frac{\partial u_j}{\partial x_j}\right) - \frac{2}{3}\left(\rho k + \frac{\mu_t \partial u_k}{\partial x_k}\right)\delta_{ij} \tag{6}$$

where μ_t is the turbulent viscosity and δ_{ij} is the Kronecker delta. The $\delta_{ij} = 1$ if i = j and $\delta_{ij} = 0$ if $i \neq j$.

The turbulent heat flux in Eq. (3) is represented as follows (Subasi et al., 2016).

$$-\overline{\rho T' u_j \prime} = \frac{\mu_t}{\mathrm{Prt}}\left(\frac{\partial T}{\partial x_j}\right) \tag{7}$$

The turbulent flow is quite complicated in which fluid flow takes place due to mean velocity and velocity fluctuations due to the formation of eddies (Xiang et al., 2022). The mean velocity has been represented by the turbulent kinetic energy (k) and velocity fluctuations have been represented by the dissipation of energy (ε). The two transport equations have been used for calculating the mean kinetic energy (k) and dissipation rate (ε) which are represented below.

Turbulent kinetic energy (k) model equation (Khattak & Ali, 2019)

$$\frac{\partial}{\partial x_i}\left(\rho k u_i\right) = \frac{\partial}{\partial x_j}\left(\alpha_k \mu_{eff}\left(\frac{\partial k}{\partial x_j}\right)\right) + G_k - \rho\varepsilon + S_k \tag{8}$$

$$\frac{\partial}{\partial x_i}\left(\rho \varepsilon u_i\right) = \frac{\partial}{\partial x_j}\left(\alpha_k \mu_{eff}\left(\frac{\partial \varepsilon}{\partial x_j}\right)\right) + C_{1\varepsilon}\left(\frac{\varepsilon}{k}\right)G_k - C_{2\varepsilon}^{*}\rho\left(\frac{\varepsilon^2}{k}\right) \tag{9}$$

S_K and G_K represent turbulent kinetic energy and energy generation due to mean velocity gradient. It is represented by the following equation (Khattak & Ali, 2019).

$$G_k = \mu_t \left(\frac{\partial u_i}{\partial x_j} + \frac{\partial u_j}{\partial x_i} \right) \left(\frac{\partial u_i}{\partial x_j} \right) \tag{10}$$

The turbulent viscosity has been determined by determining the k and ε (Maheswari & Prajapati, 2022).

$$\mu_t = \frac{\rho C_k k^2}{\varepsilon} \tag{11}$$

The effective viscosity determined by following equation (Maheswari & Prajapati, 2022)

$$\mu_e = \mu + \mu_t \tag{12}$$

where μ_e is the effective viscosity.

The $C^*_{2\varepsilon}$ is the constant determined by following equation (Maheswari & Prajapati, 2022).

$$C^*_{2\varepsilon} = C_{2\varepsilon} + \frac{C_\mu \eta^3 \left(1 - \frac{\eta}{\eta_O}\right)}{1 + \beta \eta^3} \tag{13}$$

where η is the ratio of the turbulence kinetic energy to the rate of dissipation of turbulence kinetic energy (Maheswari & Prajapati, 2022).

$$\eta = \frac{S_k}{\varepsilon} \tag{14}$$

The values of constants C_μ, $C_{1\varepsilon}$, $C_{2\varepsilon}$, η_O, β, α_k and α_E are as follows namely 0.085, 1.42, 1.68, 4.38, 0.012, 1.393 and 1.393 (Maheswari & Prajapati, 2022).

The base of the heat sink has the dimensions of 10 mm × 10 mm x 1 mm and the fin length, height and thickness is 10 mm × 10 mm × 0.8 mm. The length of the entrance and exit region is provided to be 15 mm and 50 mm. The gap of the fins is provided to be 1.5 mm as shown in Fig. 4a. Figure 4b represents the meshing on the enclosure and the heat sink. The number of the element and nodes in the geometry are 52,732 and 53,317. The transition ratio represents the growth of the adjacent elements on the one another, if the transition ratio increases then the gap between the elements increases. In the meshing the transition ratio, maximum layer and growth rate has to be measured as 0.272, 5 and 1.2.

The minimum and maximum element size of the mesh is 0.25 mm and 1 mm. Figure 5a represents the skewness of the meshing elements, the maximum skewness of the Fig. 5a is 0.8871. The skewness represents the similarity of the mesh elements with the ideal elements. The skewness of the elements varies between the 0–1. The 0 represents the worst quality of the mesh and 1 represents the maximum quality of the mesh. The average skewness of the meshing in Fig. 5a is 0.59. The 2nd criteria of the mesh quality are orthogonality. The orthogonality depicted, the angular deviation between the faces of the actual mesh and ideal geometry. The minimum, maximum and average orthogonality of the meshing elements are 0.11282, 1 and 0.70 as presented in Fig. 5b.

Figure 5c represents the quality of the mesh. Figure 5c represents the minimum mesh quality is 0.20937 and maximum mesh quality is 1 which shows good quality of mesh. Figure 5d represents the aspect ratio, the aspect ratio measures the twisting of the mesh element. It is simply measure by dividing the node distance from the centroid of the mesh and the centroid to the face centroid distance. The most of the element have the aspect ratio less than the 2.0 shows the good quality of the mesh (Verma et al., 2023).

Optimization techniques

Optimization is the important technique used for maximizing the performance of the system in every field of the work like engineering and medical sciences. The heat transfer problem solution of the heat sink requires to maximize the heat transfer variables and minimize the pumping losses variables. In this research, a method has been presented which optimized the heat sink, flow and heat transfer variables like flow velocity, air inlet temperature and the heat flux.

The Response Surface Methodology (RSM) has been preferably used for optimization. The MINITAB 17 and Design Expert software were used for ANOVA analyses and surface and contour plots of the responses. The Box-Behenken Design (BBD) technique has been selected in RSM for defining the input and output variables. The best thing with the BBD is that it requires only three level as compare to five level design in Central Composite Design (CCD) for every input variable. it requires the mid-level between the low and high values of every factor (Singh et al., 2023a). The coded value of mid-level is $0, +1$ represents the maximum value of the factor and -1 represents the minimum value of the input variables. Table 2 represents the code and coded values of the input variables. Based on three input variables total number of the runs for design matrix is 17. Table 3 represents the total number of runs and corresponding values of the responses (AlShaar et al., 2022; Kumar et al., 2023).

Tables 4, 5 and 6 represent the model analysis by ANOVA. Whether the model is significant or not that has been tested by the P and F values of the model. The F test is the ratio of the variability between the treatment and error. So, larger F values justified the accuracy of the model ("Experimental and Computational Investigation of Flow Fields using Accelerated Erosion Test Ring (AETR)" 2021). In Tables 4, 5 and 6, the F values of chip temperature, pressure drop, fan power, friction factor and Nusselt Number are 3983.59, 365.70, 87.04, 474.69 and 58.98 implies that model is significant. The P values represent the probability

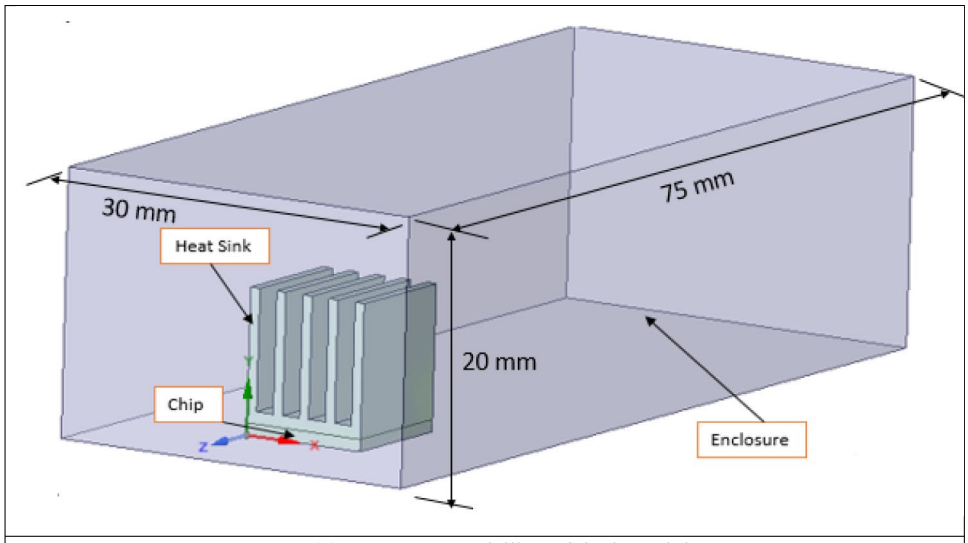

(a) Geometry modelling of the heat sink

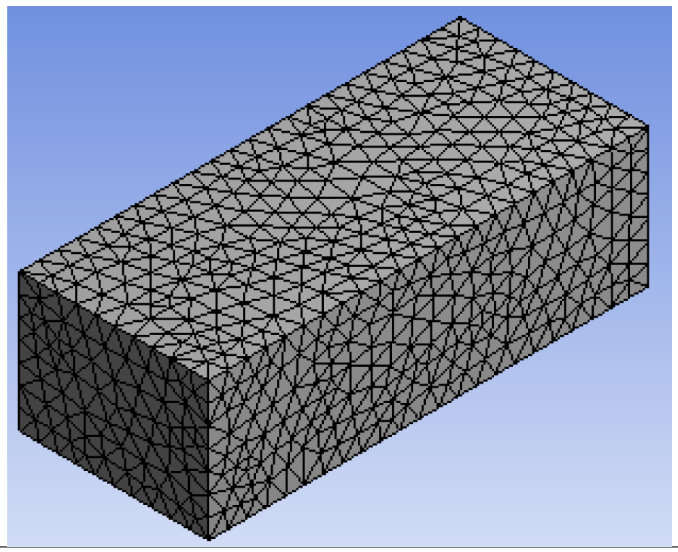

(b) Meshing on the heat sink

Fig. 4 Geometry and Meshing on the heat Sink

of rejection of the null hypothesis in ANOVA analysis (Singh & Yadav, 2022). In ANOVA analysis, the chance of rejection of null hypothesis is 5% so that the *P* values less than 0.05 shows the significance of model. The Tables 4, 5 and 6 the *P* values of the chip temperature, pressure drop, fan power, friction factor, and Nusselt Number are less than 0.0001 showing the significance of the model (Singh et al., 2023b).

Table 7 represents the fit statics of ANOVA analysis. The accuracy of the predicted model and actual values are measured by the R^2, adjusted R^2, Predicted R^2 and adequate precision. For the chip temperature, the predicted R^2 and adjusted R^2 are 0.9998, and 0.9996 shows very little variation. The adequate precision shows the ratio between the signal and the noise present in the model and values of the adequate precision greater than 4 are desirable. The adequate precision values for chip temperature, pressure drop, fan power, friction factor, and Nusselt Number is 242.0344, 48.2841, 23.5553, 55.0106and 22.4582. The models of the responses in term of input variables are represented by 2nd order polynomials. The following model equations of the responses represented in terms of the input variables.

$$T_{chip} = 279.76 - 3.14V + 0.9052T_{air} + 0.000002q_{gen} + 0.523V^2 + 0.00088T_{ain}^2 \quad (15)$$

$$P = -0.1 + 0.13V + 0.19V^2 \quad (16)$$

$$F_{Power} = 0.000274 - 0.000302V + 0.00011V^2 \quad (18)$$

Fig. 5 Mesh quality check by various parameters

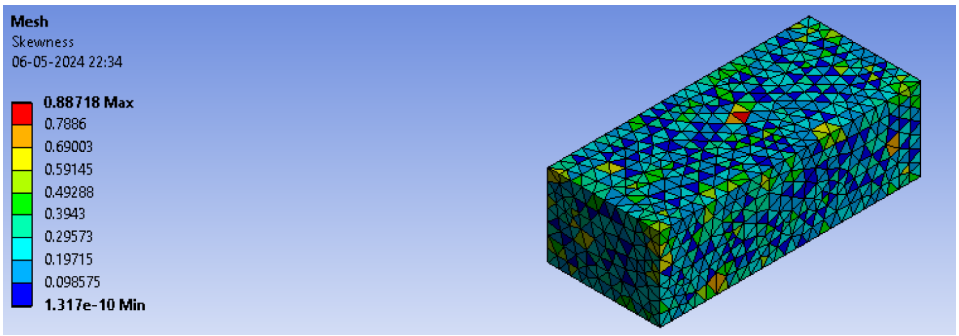

(a). Skewness in the meshing

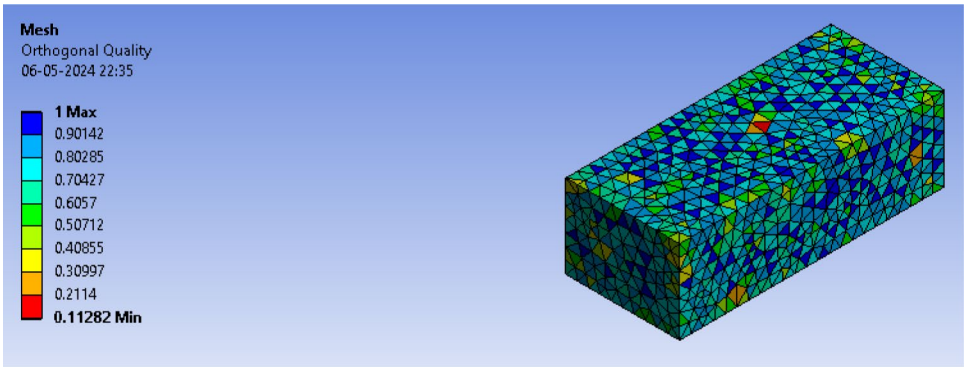

(b). Orthogonality in the meshing

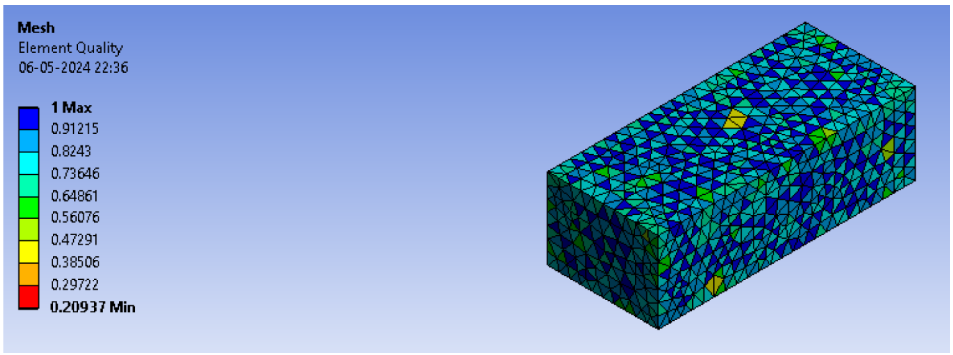

(c). Element quality in meshing

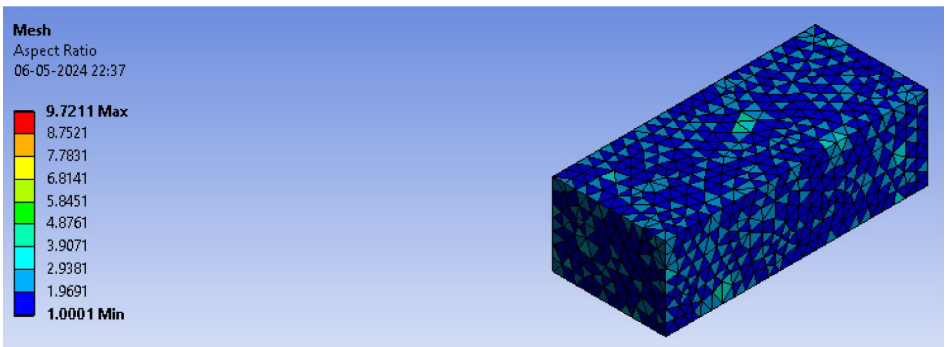

(d). Aspect ratio of the mesh element

Table 2 Code and coded values of the input variables

Input Variables	Coded level		
Code	–1	0	1
Air Inlet velocity (m/s)	2	3	4
Atmospheric Temperature (°C)	25	30	35
Heat Flux (W/m^3)	1×10^7	1.75×10^7	2.5×10^7

$$f = 0.1508 - 0.007387V + 0.000543V^2 \quad (19)$$

$$Nu = 3.864 + 0.784V + 0.0323T_{ain} - 0.0691V^2 - 0.000299T_{ain}^2 \quad (20)$$

where T_{air} is the inlet air temperature (°C), V is the inlet air velocity (m/s), q_{gen} is the heat generated (W/m^3).

Table 3 Total number of runs and corresponding responses

S. No.	V	T_{ain}	q	T_{chip} (K)	P (Pa)	F_{Power} (W)	f	h	Nu
1	3	15	2.50×10^7	333.43	2	0.00036	0.13354667	46.63535	6.369878
2	3	25	1.75×10^7	329.76	2	0.00036	0.13354667	46.69556	6.378101
3	2	15	1.75×10^7	322.25	0.92	0.0001104	0.1382208	43.30075	5.914408
4	4	35	1.75×10^7	338.49	3.46	0.0008304	0.1299576	48.64057	6.643768
5	3	25	1.75×10^7	329.76	2	0.00036	0.13354667	46.69556	6.378101
6	4	25	1.00×10^7	315.36	3.46	0.0008304	0.1299576	48.81668	6.667823
7	3	25	1.00×10^7	306.8	2	0.00036	0.13354667	45.07753	6.157097
8	3	35	2.50×10^7	353.43	2	0.00036	0.13354667	46.63535	6.369878
9	2	35	1.75×10^7	342.25	0.92	0.0001104	0.1382208	43.30075	5.914408
10	3	35	1.00×10^7	326.08	2	0.00036	0.13354667	46.87266	6.402291
11	4	15	1.75×10^7	318.49	3.46	0.0008304	0.1299576	48.64057	6.643768
12	2	25	2.50×10^7	346.99	0.92	0.0001104	0.1382208	43.24646	5.906992
13	2	25	1.00×10^7	317.51	0.92	0.0001104	0.1382208	43.43709	5.93303
14	3	25	1.75×10^7	329.76	2	0.00036	0.13354667	46.69556	6.378101
15	4	25	2.50×10^7	341.62	3.46	0.0008304	0.1299576	48.57047	6.634194
16	3	25	1.75×10^7	329.72	2	0.00036	0.13354667	46.75444	6.386144
17	3	25	1.75×10^7	329.73	2	0.00036	0.13354667	46.73971	6.384131

Table 4 *P*-value and F value for checking the effectiveness of the regression analysis on chip temperature and pressure drop

Sources	DF	Chip Temperature				Pressure drop of air			
		Adj. SS	Adj. MS	F-value	*P*-value	Adj. SS	Adj. MS	F-value	*P*-value
Model	9	2322.79	258.087	3983.53	< 0.0001	12.90	4.30	365.70	< 0.0001
Linear	3	1101.11	2318.73	35,789.848	< 0.0001	12.90	12.90		
V	1	28.27	28.27	436.422	< 0.0001	12.90	12.90	1097.11	< 0.0001
Ta	1	785.66	785.66	12,126.595	< 0.0001	0.000	0.000	0.000	1.0000
q	1	1504.80	1504.80	23,226.469	0.0001	0.000	0.000	0.0000	1.0000
Square	3	47.23	1.2552	19.3803	0.4314				
V*V	1	1.18	1.180	42.0115	0.0037	–	–	–	–
Ta*Ta	1	0.03760	0.0376	40.008	0.0539	–	–	–	–
S*S	1	0.0376	0.0376	2.00035	0.4711	–	–	–	–
2-way Interaction	3	32.94	2.77216	14.43	1.116				
V*Ta	1	25.00	0.000	10.95	1.0000	–	–	–	–
V*S	1	7.94	2.592	3.48	0.0004	–	–	–	–
Ta*S	1	0.000	0.1296	0.000	0.2002	–	–	–	–
Error	7	15.98	0.0003	–	–	0.1529	3.21e-07	–	–
Lack of Fit	3	0.452	0.1506	–	< 0.0001	0.1529	0.0170	30,784.03	0.000
Pure Error	4	0.0015	0.000	–	–	0.00	0.0000	–	–
Total	16	2323.239	–	–	–	13.06	–	–	–

Table 5 *P*-value and F value for checking the effectiveness of the regression analysis on fan power and friction factor

Sources	DF	Fan power				Friction factor			
		Adj. SS	Adj. MS	F-value	*P*-value	Adj. SS	Adj. MS	F-value	*P*-value
Model	3	1.037E-06	3.456E-07	87.04	< 0.0001	0.0001	0.0000	474.69	< 0.0001
Linear	3	1.037E-06	1.037E-06	261.11	< 0.0001	0.0001	0.0001	1424.08	< 0.0001
V	1	1.037E-06	1.037E-06	261.11	< 0.0001	0.0001	0.0001	1424.08	< 0.0001
Ta	1	0.0000	0.0000	0.0000	0.0001	0.000	0.000	0.000	1.0000
q	1	0.0000	0.0000	0.0000	0.0001	0.000	0.000	0.0000	1.0000
Square	–	–	–	–	–	–	–	–	–
V*V	–	–	–	–	–	–	–	–	–
Ta*Ta	–	–	–	–	–	–	–	–	–
S*S	–	–	–	–	–	–	–	–	–
2-way Interaction	–								
V*Ta	–	–	–	–	–	–	–	–	–
V*S	–	–	–	–	–	–	–	–	–
Ta*S	–	–	–	–	–	–	–	–	–
Error	13	5.162E-08	3.971E-09	–	–			–	–
Lack of Fit	9	5.162E-08	5.736E-09	–	–	–	–	–	–
Pure Error	4	0.0000	0.0000	–	–			–	–
Total	16	1.088E-06		–	–		–	–	–

Experimental setup

Figure 6 shows the experimental set-up of the heat sink cooled by air. The experimental setup consists of the transformer, temperature display meter, speed regulator, multimeter, and a duct having the compressor for air flow. The transformer supplies the optimum voltage and current to the micro heater to supply the heat to the heat sink, the measurement of current and voltage has been done by the multimeter. The speed regulator is used to regulate the speed of the compressor at varying mass flow rates. The temperature display meter measured the temperature of the inlet air, outlet air, and heat sink base, mid, and top surface. Figure 7 represents the location of the various instruments in the experimental setup. At the time of the experiment, the experimental setup started before 15 min. The current, voltage, air flow velocity, temperature at various locations, and pressure drop have been noted at various heat flux. Based on the experimental data, pan power, heat transfer coefficient and Nusselt Number have been determined by the model equations.

Results and discussion

CFD results

Temperature contour

Figure 8 represents the temperature contour of the heat sink at various conditions of the air inlet velocity, air inlet temperature and heat generation inside the heat sink. Figure 8a–j represents that if the heat generation and inlet air temperature of the heat sink enhanced then the chip temperature increases, on other hand if the inlet air velocity increased then the chip temperature is reduced. If the inlet air temperature is increasing, then heat transfer in air by heat sink is reduced which increase the temperature of heat sink. If inlet air temperature increases, then the convection heat transfer coefficient increases which enhances the heat transfer rate and reduced the heat sink temperature.

Pressure contour

Figure 9, pressure contour plot shows that if the inlet air Velocity increased then the pressure drop on heat sink increased since dynamic pressure is directly proportional to the square of velocity. The effect of the heat generation and inlet air temperature is neglected on pressure drop since air properties are not much changed due to lower working air temperature. Figure 9a–c show that the maximum pressure drop of the air occurs at the base of the heat sink represented by the red colour. The maximum pressure drops in Fig. 9a–c

Table 6 *P*-value and F value for checking the effectiveness of the regression analysis on Nusselt Number

Sources	DF	Nusselt number			
		Adj. SS	Adj. MS	F-value	*P*-value
Model	9	1.12	0.1245	58.98	< 0.0001
Linear	3	1.07	1.037E-06	261.11	< 0.0001
V	1	1.07	1.07	505.03	< 0.0001
Ta	1	0.0075	0.0075	3.56	0.1012
q	1	0.0018	0.0018	0.8625	0.3840
Square	3	0.0277	0.0277	13.11	–
V*V	1	0.0210	0.0210	9.93	0.0161
Ta*Ta	1	0.0041	0.0041	1.95	0.2052
S*S	1	0.0026	0.0026	1.23	0.3037
2-way Interaction	3	0.0150	0.0150	7.1268	
V*Ta	1	0.0000	0.0000	0.0000	1.0000
V*S	1	0.0000	0.0000	0.0068	0.9365
Ta*S	1	0.0150	0.0150	7.12	0.0321
Error	7	0.0148	0.0021	–	–
Lack of Fit	3	0.0147	0.0049	319.40	< 0.0001
Pure Error	4	0.0001	0.0000	–	–
Total	16	1.14		–	–

Table 7 Fit statics analysis of the responses of the heat sink

S. No.	Statics measurement variables	Chip temperature	Pressure drop	Fan power	Friction factor	Nusselt number
1	R^2	0.9998	0.9883	0.9526	0.9910	0.9870
2	Adjusted R^2	0.9996	0.9856	0.9416	0.9889	0.9702
3	Predicted R^2	0.9969	0.9784	0.9127	0.9833	0.7925
4	Adeq Precision	242.0344	48.2841	23.5553	55.0106	22.4582

are 2.0 Pa, 0.92 Pa, and 3.46 Pa. As the air reaches the inlet of the heat sink, the air strikes the heat sink surface giving the maximum pressure and when air further moves and passes through the gap between the two fins, the air velocity increases, and the pressure is reduced. So blue colour region gives the negative pressure and red colour gives the maximum pressure at the inlet of the heat sink. The intensity of the negative pressure also depends on the air inlet velocity. The higher pressure drop across the heat sink leads to higher blower power. As the inlet air velocity increases from 2 m/s to 4 m/s in Fig. 9b and c, the maximum pressure drops from – 3.23 Pa to – 14.32 Pa.

Velocity contour

Figure 10 represents the velocity contour of the air through the heat sink. Figure 10a–c show that air velocity is maximum above the heat sink represented by the red color on all three contour plots. The blue colour of the airflow velocity represents the zero velocity due to no-slip boundary conditions and consideration of the adiabatic wall of the base of the panel of the heat sink. The Fig. 10a–c contour plots clearly show that the velocity of the air flow increased due to the reduction of the flow area in between the two consecutive fins. This is due to satisfying the boundary conditions of the conservation of the mass. The maximum velocity of air is 3.61 m/s in Fig. 10a and 2.43 m/s in Fig. 10b due to in Fig. 10a the boundary layer is narrow and in Fig. 10b the boundary layer is broader.

Fig. 6 Experimental setup of the heat sink cooled by atmospheric air

Optimization plots

Chip temperature contour and surface plot

Pressure variation with input variables

Nusselt number variation with input variables

Optimization plots

Figure 11a–e represent the chip temperature surface plot and contour plot with input variables. Figure 11a shows that chip temperature increases due to both heat generation and inlet air temperature.

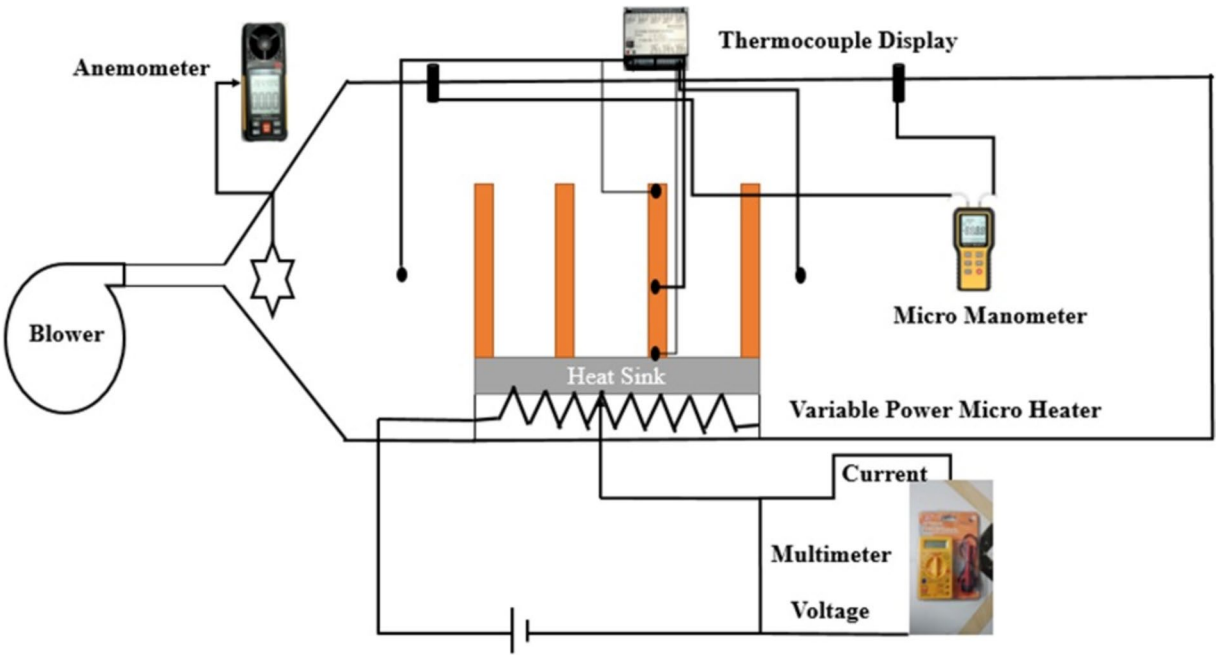

Fig. 7 Schematic representation of the Experimental setup

Fig. 8 Numerical simulation temperature plot of heat sink at various flow conditions

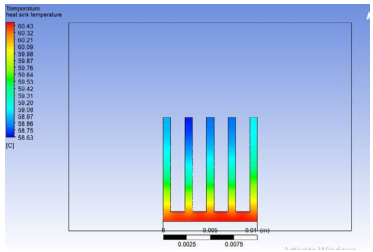

(a) Temperature contour at V = 3 m/s, T_{ain} = 15°C and $q_{gen} = 2.5 \times 10^7$ W/m^3.

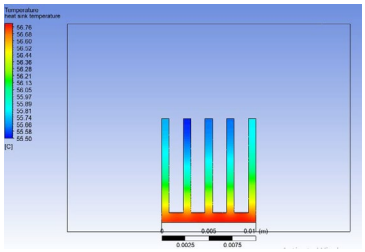

(b) Temperature contour at V = 3 m/s, T_{ain} = 25°C and $q_{gen} = 1.75 \times 10^7$ W/m^3.

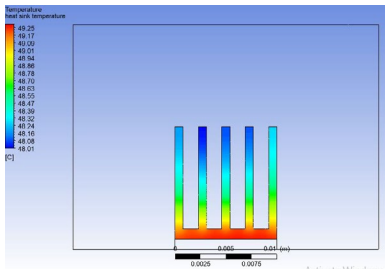

(c) Temperature contour at V = 2 m/s, T_{ain} = 15°C and $q_{gen} = 1.75 \times 10^7$ W/m^3.

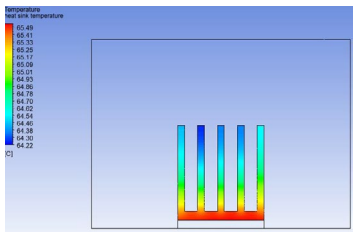

(d) Temperature contour at V = 4 m/s, T_{ain} = 35°C and $q_{gen} = 1.75 \times 10^7$ W/m^3.

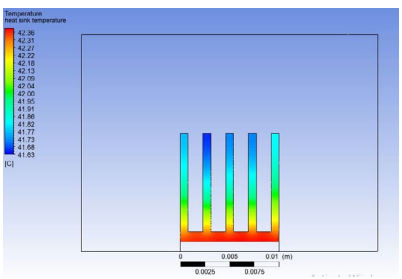

(e) Temperature contour at V = 4 m/s, T_{ain} = 25°C and $q_{gen} = 1 \times 10^7$ W/m^3.

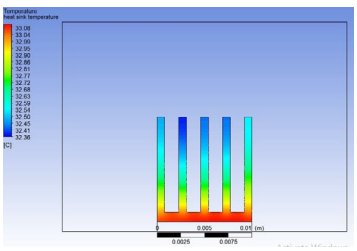

(f) Temperature contour at V = 3 m/s, T_{ain} = 15°C and $q_{gen} = 1.75 \times 10^7$ W/m^3.

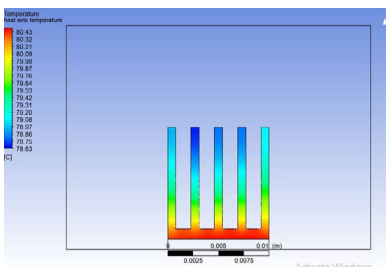

(g) Temperature contour at V = 3 m/s, T_{ain} = 35°C and $q_{gen} = 2.5 \times 10^7$ W/m^3.

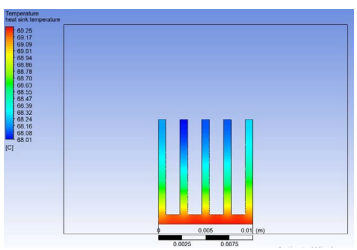

(h) Temperature contour at V = 2 m/s, T_{ain} = 35°C and $q_{gen} = 1.75 \times 10^7$ W/m^3.

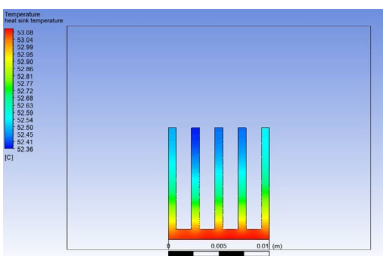

(i) Temperature contour at V = 3 m/s, T_{ain} = 35°C and $q_{gen} = 1 \times 10^7$ W/m^3.

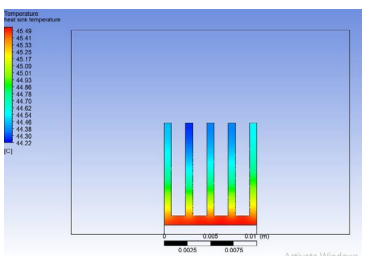

(j) Temperature contour at V = 4 m/s, T_{ain} = 15°C and $q_{gen} = 1.75 \times 10^7$ W/m^3.

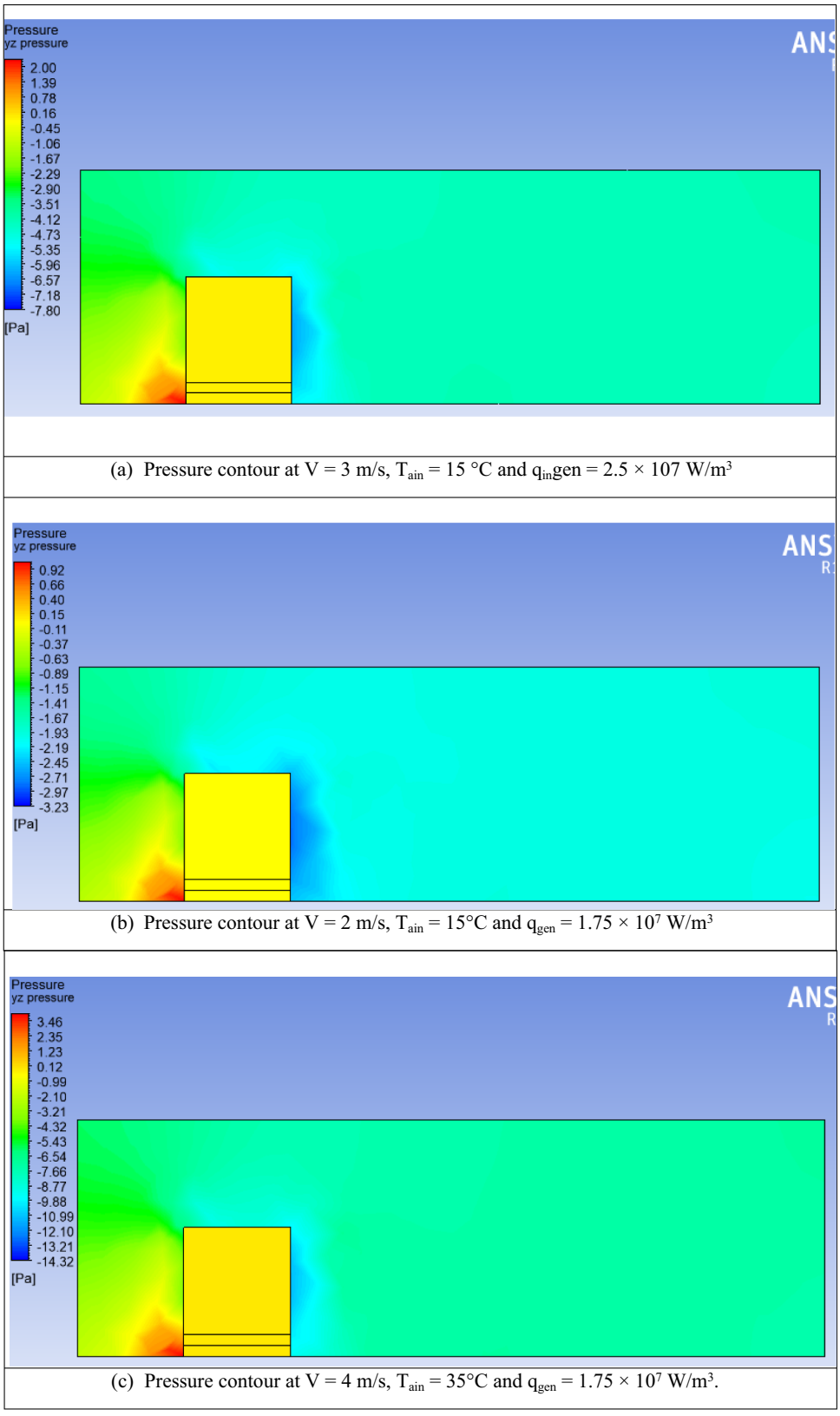

(a) Pressure contour at V = 3 m/s, T_{ain} = 15 °C and $q_{in}gen$ = 2.5 × 107 W/m^3

(b) Pressure contour at V = 2 m/s, T_{ain} = 15°C and q_{gen} = 1.75 × 10^7 W/m^3

(c) Pressure contour at V = 4 m/s, T_{ain} = 35°C and q_{gen} = 1.75 × 10^7 W/m^3.

Fig. 9 Pressure contour of heat sink at various flow conditions

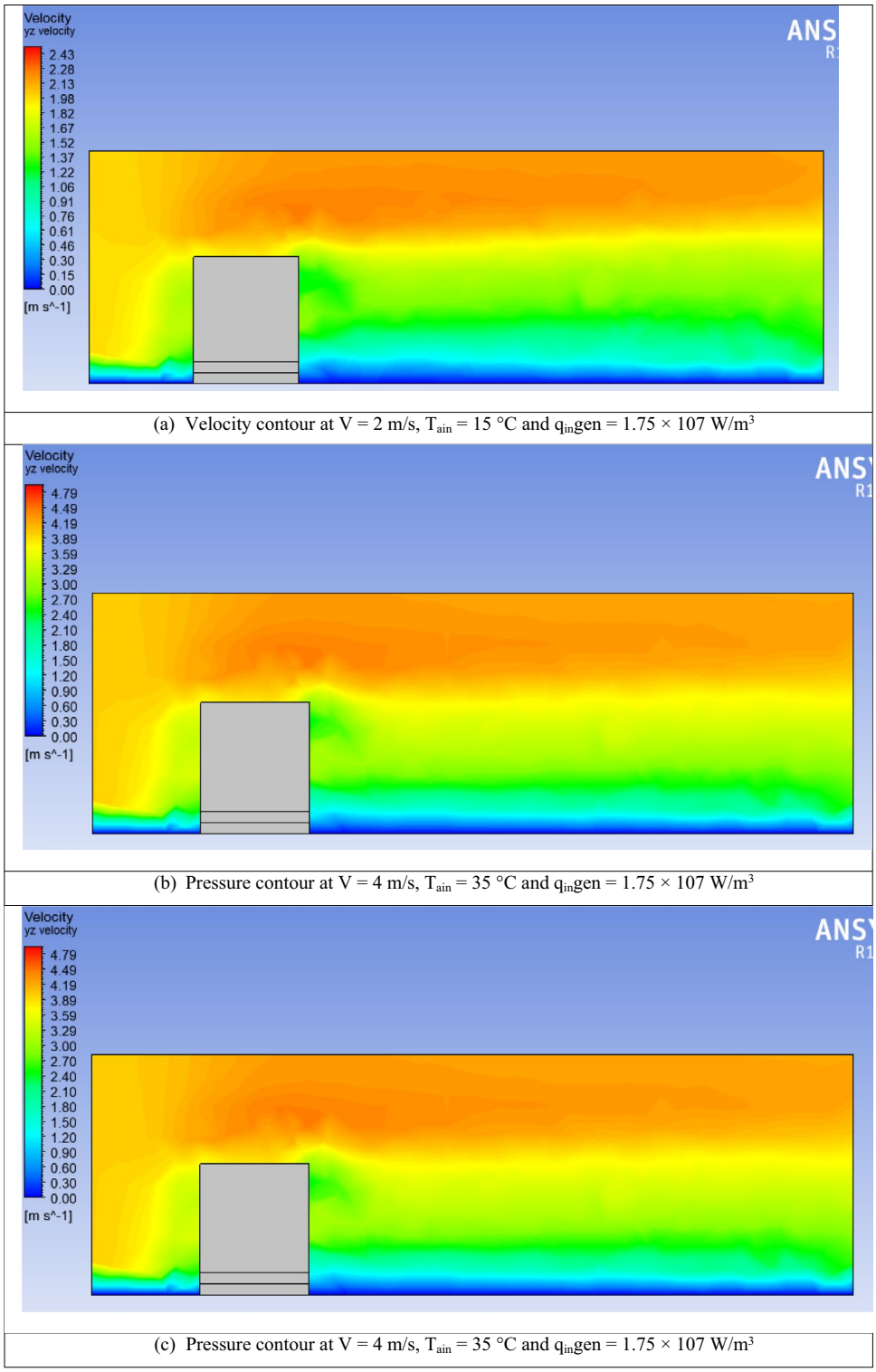

Fig. 10 Velocity contour of heat sink at various flow conditions

Figure 11b red color represents the chip temperature more than 350 K, the region of maximum inlet air temperature, and the maximum heat generation. Figure 11c represents the surface plot between the chip temperature and the inlet air velocity and the heat generated inside the chip. It is seen from Fig. 11c that if the inlet air velocity increased then the chip temperature is reduced. Figure 11d shows the contour plot between the chip temperature and inlet air velocity and the heat generated inside the chip. Figure 11e and f represent the surface and contour plot of the chip temperature with inlet air temperature and the inlet air temperature (Jaffar et al., 2022).

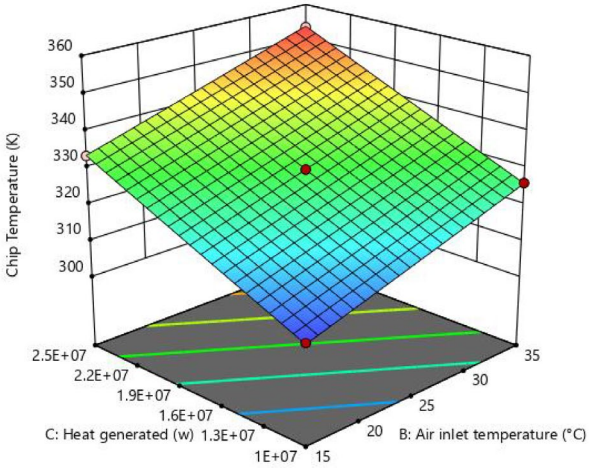

(a) Chip temperature variation with Heat Generated and Air inlet Temperature

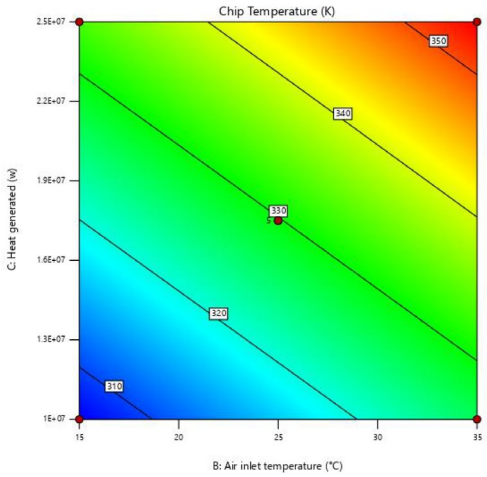

(b) Contour plot of chip temperature with heat generated and air inlet temperature

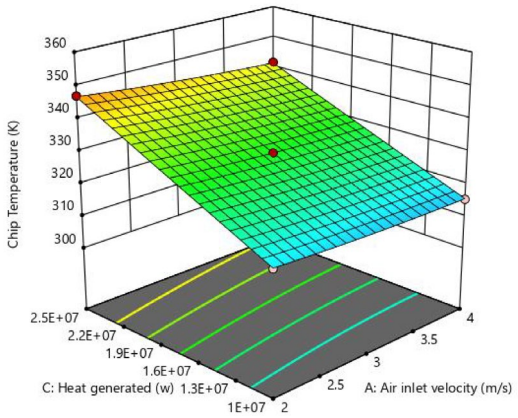

(c) Surface plot of chip temperature with heat generated and air inlet velocity

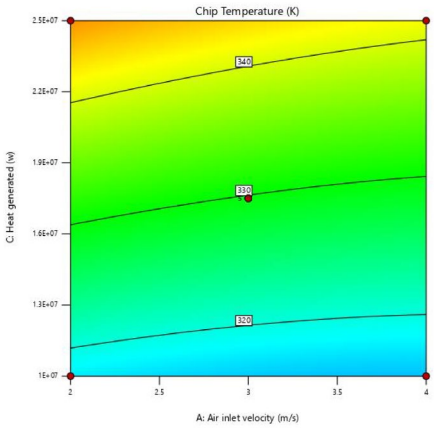

(d) Chip temperature contour plot with heat generated and air inlet velocity

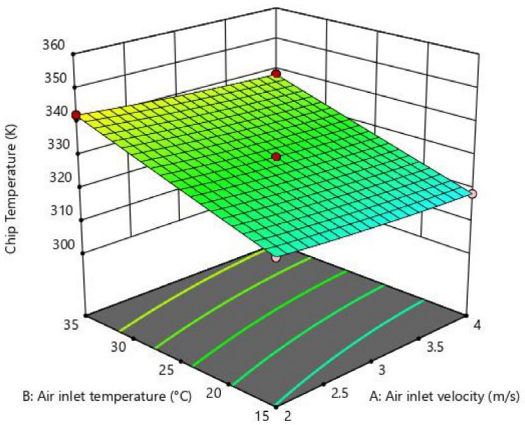

(e) Surface plot of chip temperature with air inlet temperature and air inlet velocity

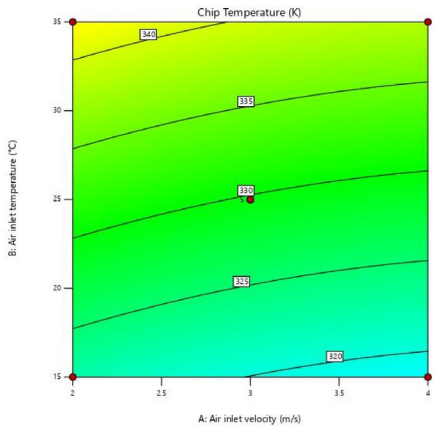

(f) Contour plot of chip temperature with air inlet velocity and air inlet temperature

Fig. 11 Surface and contour plots of the chip temperature

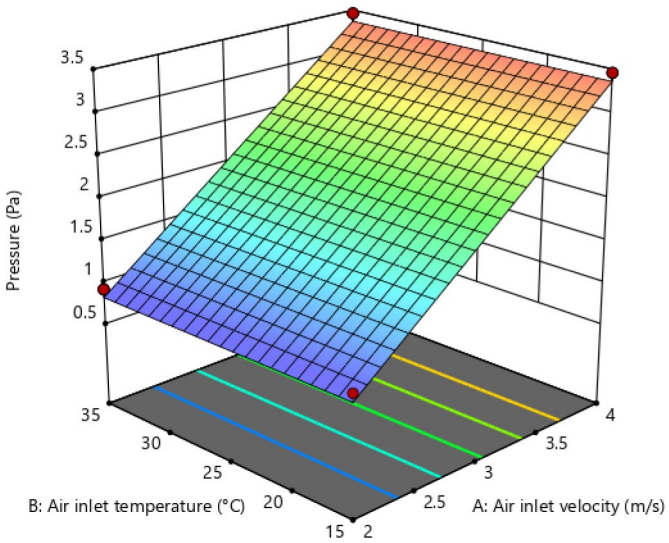

(a) Pressure variation with air inlet temperature and air inlet velocity

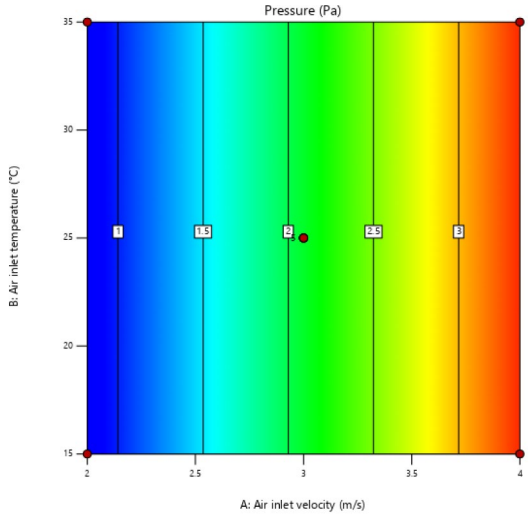

(b) Contour plot of pressure with air inlet temperature and air inlet velocity

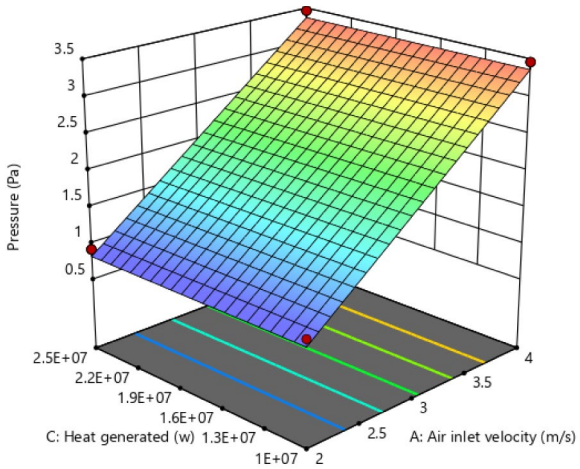

(c) Surface plot of pressure with heat generated and air inlet velocity

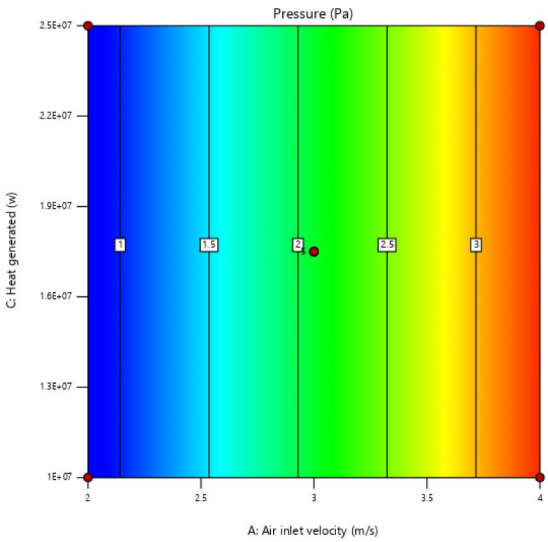

(d) Pressure contour plot with Heat generated and air inlet velocity

Fig. 12 Surface and contour plot of the pressure drop

Figure 12a–d depicted pressure variation with the input variables namely inlet air temperature, inlet air velocity, and heat generation inside the chip. Figure 12a shows the pressure variation with the inlet air temperature and inlet air velocity. Figure 12a shows that as the inlet air velocity increased then pressure drop increased. The pressure through the inlet air temperature is neglected due to less variation in the air temperature. The contour plot of the pressure with the inlet air velocity represents the vertical line as presented in Fig. 12b. Figure 12c and d represents the constant pressure with the heat generation but variation with the velocity of air is noted (Herlambang et al., 2022).

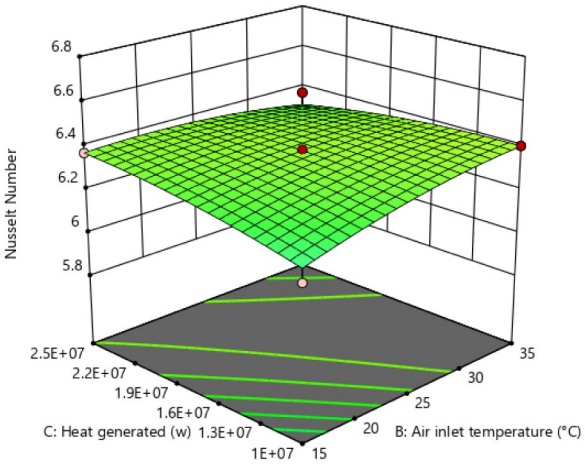

(a) Nusselt Number variation with heat generated and air inlet Temperature

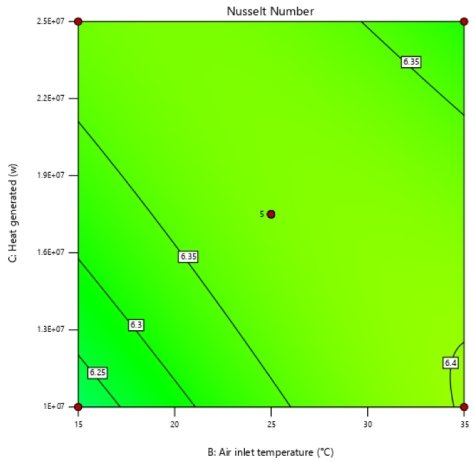

(b) Contour plot of Nusselt Number with heat generated and air inlet temperature

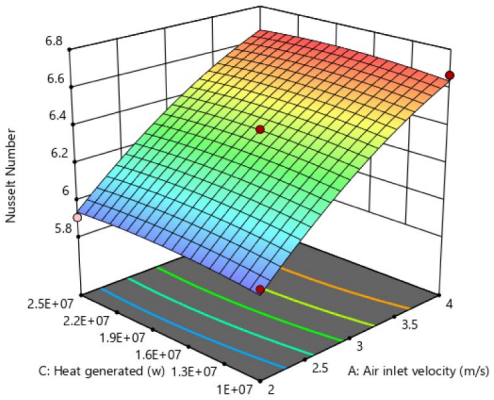

(c) Surface plate of Nusselt Number with heat generated and air inlet velocity

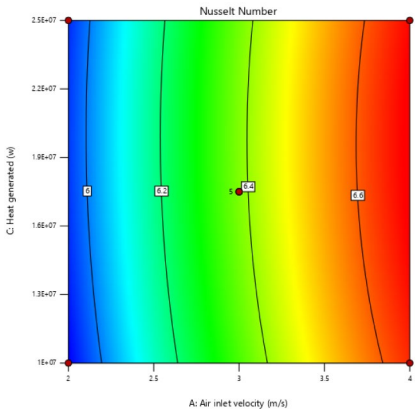

(d) Nusselt Number contour plot with heat generated and air inlet velocity

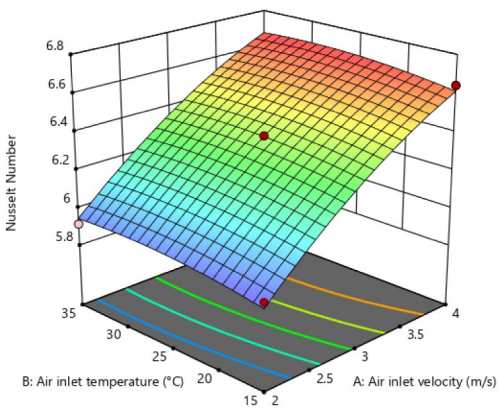

(e) Surface plot of Nusselt Number with air inlet temperature and air inlet velocity

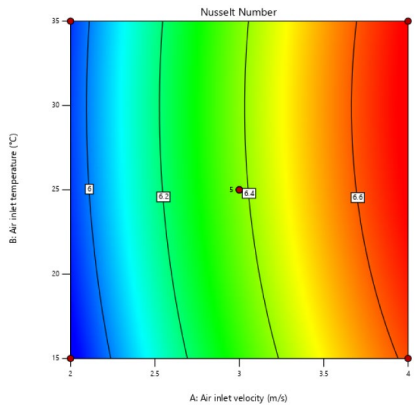

(f) Contour plot of Nusselt Number with air inlet velocity and air inlet temperature

Fig. 13 Nusselt Number variation with input variables

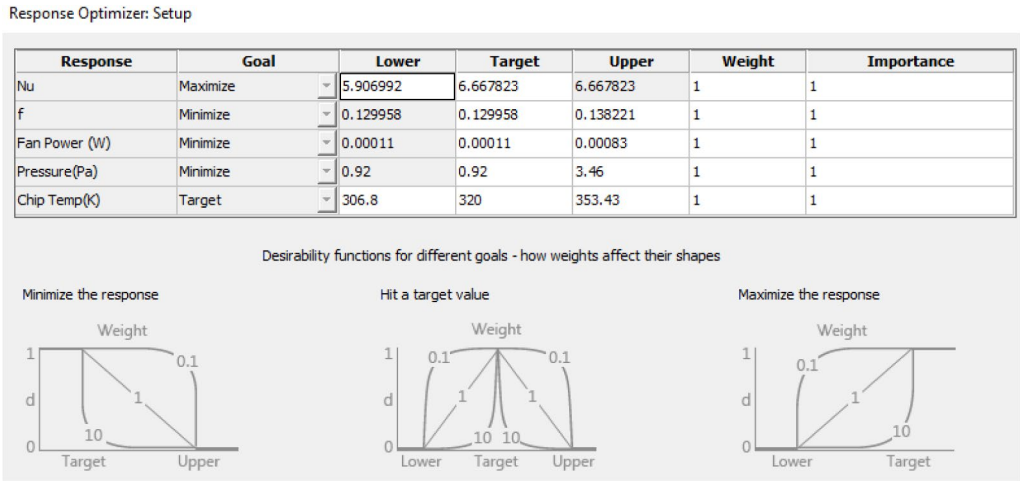

(a) Optimizer setup of responses

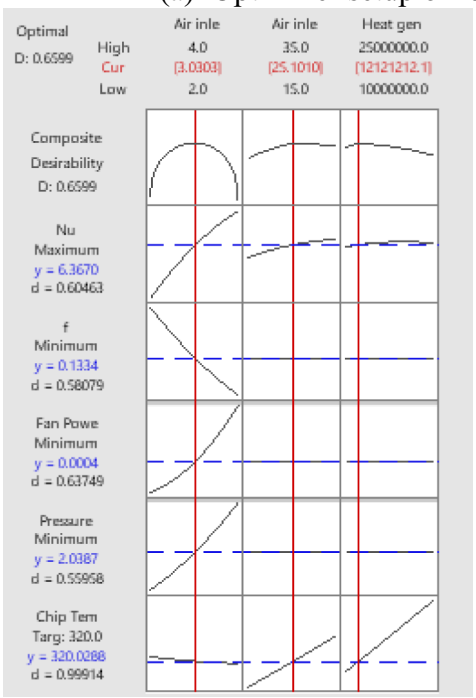

(b) Optimum values of the responses with input variables

Fig. 14 Optimization plots of the responses with input variables

Figure 13a represents the Nusselt Number variation with the heat generation and the inlet air temperature.

It is to be noted from Fig. 13a that if the heat generation and inlet air temperature increased then the Nusselt Number initially increased and then started to decrease, the main reason behind this change in curvature is that if the temperature of the air increased then Reynolds Number increases and due to that Nusselt Number increased. The contour plot of Nusselt Number in Fig. 13b also represents the same behavior (Choudhary et al., 2020).

Figure 13c represents the surface plot of the Nusselt Number variation with the heat generation and inlet air velocity. Figure 13c shows that if the inlet air velocity increased the Nusselt Number increased due to incensement of the Reynolds Number. Figure 13d contour plot red colour shows the maximum Nusselt Number at higher inlet air velocity at all values of the heat generation. Figure 13e and f also shows the Nusselt Number variation with the inlet air velocity and the inlet air temperature. Figure 13e and f both shows that the increase in inlet air velocity enhance the Nusselt Number but the enhancement in the inlet air temperature does not much change the Nusselt Number.

Figure 14a and b represent the optimization responses with the weight given to the inputs and the optimization

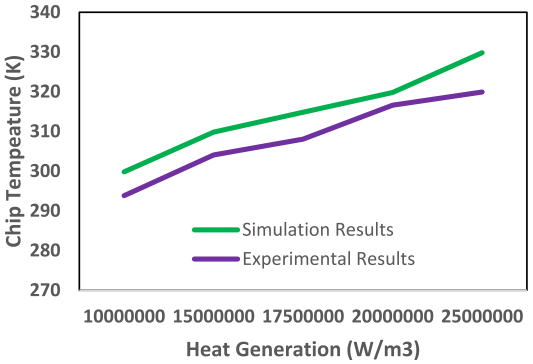

(a) Chip temperature variation with the heat generation

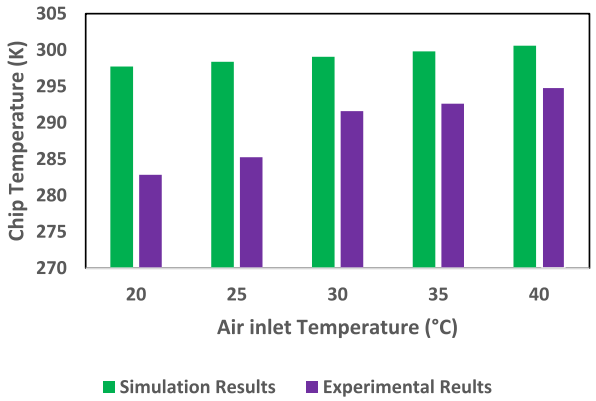

(b) Chip Temperature variation with the air inlet temperature

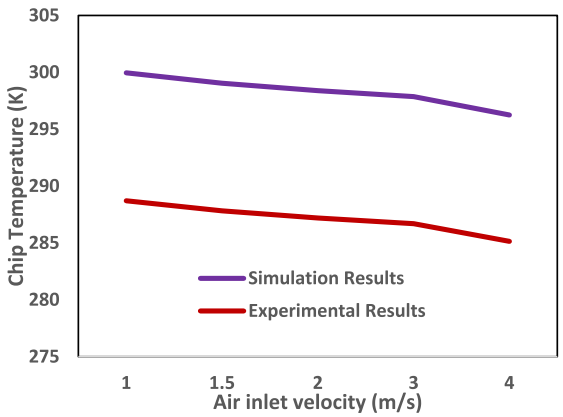

(c) Chip Temperature variation with air inlet velocity

Fig. 15 Validation of simulation results with experimental results

plots of the responses. Figure 14a represents the responses with the goal, upper, lower, and target values of the responses. Figure 14b represents the composite desirability of the optimization is 0.6599, the desirability represents the correlation between the responses and the input variables. The desirability 1 represents the perfect correlation between the input and responses. Figure 14b shows that the optimum value of the input variables like inlet air velocity 3.033 m/s, air inlet temperature 25.1010 °C, and the heat generation 1.12×10^7 W/m^3. On which responses are chip temperature 320 K, pressure drop 2.03 Pa, Nusselt Number 6.3670, friction factor 0.1334, and fan power 0.0004 W.

Validation of the simulation results with experimental results

Figure 15 represents the validation of simulation results with the experimental results. Figure 15a shows the chip temperature variation with the heat generation at an inlet air temperature of 35 °C and inlet air velocity of 4 m/s; if the heat generation increases, the chip temperature increases. Figure 15a shows that at heat generation of 2.5×10^7 W/m^3, the chip temperature is found to be 330 K and 320 K due to simulation and experimental observation respectively at 35 °C inlet air temperature and 4 m/s inlet air velocity. Figure 15b shows the chip temperature variation with the inlet air temperature. Figure 15b shows chip temperature enhancement due to the increase in the inlet air temperature, as the inlet air temperature is 40 °C, the chip temperature recorded to be 300 K and 294 K due to simulation and experimental results respectively at the heat generation 1×10^7 W/m^3 and inlet air velocity of 4 m/s. Figure 15c shows the chip temperature with the inlet air velocity, if the inlet air velocity increases, the chip temperature reduces. The chip temperature is found to be 296 K and 285 K respectively at inlet air velocity of 4 m/s, heat generation 1×10^7 W/m^3, and inlet air temperature of 25 °C by numerically and experimentally.

Conclusion

This study focused to determine the optimum heat flux, air inlet velocity and optimum environment conditions to avoid the failure of the electronics chip. In this study, the constant temperature to avoid the failure is considered the be 50 °C, that is the optimization constraint. So, if these optimum setting of the input variables like heat flux, inlet air velocity is maintained then the system remain safe at the time of working. In the heat sink cooling, the heat flux, inlet air velocity and the inlet air temperature are considered to be most important factor that affect the performance of the electronic chip. In these three variables, the heat flux is the big cause of the failure of the electronic chip. If the heat flux is very high then the failure of the electronic chip is 100% to avoid the failure the cooling fluid must be changed. The study reveals that the inlet air temperature also responsible to increase the

temperature of the electronic chip. The increasing the inlet air temperature increase the chip temperature.

The air inlet velocity enhances the heat transfer coefficient and heat transfer rate but air inlet velocity cannot increase after certain values otherwise noise problems can create other undesirable problems. In this research, the simulation results show that if the inlet air velocity increases then the fan power and pressure drop enhanced. If heat flux is more than 2.5×10^7 W/m^3 then chip temperature reached be more than 80 °C. To avoid the failure of electronic chip, the optimum values of the input variables namely air inlet velocity 3.03 m/s, air inlet temperature 25.1010 °C and heat flux 1.12×10^7 W/m^3 on which responses Nusselt Number 6.3670, chip temperature 320.0288 K, pressure 2.077 pa, fan power 0.004 W and friction factor 0.1334.

Acknowledgements The authors wish to thank all who assisted in conducting this work.

Funding The Authors have no funding from an outside source.

Declarations

Conflict of interest The authors want to affirm that there are no known conflicts of interest related to this publication.

Ethical approval This article does not contain any studies with human participants or animals performed by any of the authors.

References

Adhikari, R. C., Wood, D. H., & Pahlevani, M. (2020). Optimizing rectangular fins for natural convection cooling using CFD. *Thermal Science and Engineering Progress, 17*, 100484. https://doi.org/10.1016/j.tsep.2020.100484

Ahmed, H. E. (2016). Optimization of thermal design of ribbed flat-plate fin heat sink. *Applied Thermal Engineering, 102*, 1422–1432. https://doi.org/10.1016/j.applthermaleng.2016.03.119

Alsarraf, J., Moradikazerouni, A., Shahsavar, A., & Afrand, M. (2019). Hydrothermal analysis of turbulent boehmite alumina nanofluid flow with different nanoparticle shapes in a minichannel heat exchanger using two-phase mixture model. *Physica a: Statistical Mechanics and Its Applications, 520*, 275–288. https://doi.org/10.1016/j.physa.2019.01.021

AlShaar, M. W., Al-Omari, Z., Emar, W., Alnsour, M., & Abu-Rumman, G. (2022). Application of PV-Thermal Array for Pumping Irrigation Water as an Alternative to PV in Ghor Al-Safi, Jordan: A case study. *Evergreen, 9*(4), 1140–1150. https://doi.org/10.5109/6625725

Black, J. R. (1969). Electromigration—a brief survey and some recent results. *IEEE Transactions on Electron Devices, 16*(4), 338–347. https://doi.org/10.1109/T-ED.1969.16754

Bondareva, N. S., & Sheremet, M. A. (2022). Influence of PCM heat sink shape on cooling of heat-generating elements in electronics. *Applied Thermal Engineering*. https://doi.org/10.1016/j.applthermaleng.2022.118695

Choudhary, S., Sharma, A. Gupta, S., Purohit, H., Sachan, S. (2020). Use of RSM technology for the optimization of received signal strength for LTE signals under the influence of varying atmospheric conditions. *Kyushu Univ. バージョン: 権利関係: Evergreen. Joint Journal of Novel Carbon Resource Sciences and Green Asia Strategy*, *07*, 500–509, 2020, https://doi.org/10.5109/4150469.

da Silva, V. A., de Neves Gomes, L. A. C., de Lima e Silva, A. L. F., & de Lima e Silva, S. M. M. (2019). Analysis of natural convection in heat sink using OpenFOAM and experimental tests. *Heat and Mass Transfer und Stoffuebertragung, 55*(8), 2289–2304. https://doi.org/10.1007/s00231-019-02574-5

Feng, S., Shi, M., Yan, H., Sun, S., Li, F., & Jian, T. (2018). Natural convection in a cross-fin heat sink. *Applied Thermal Engineering, 132*, 30–37. https://doi.org/10.1016/j.applthermaleng.2017.12.049

Haghighi, S. S., Goshayeshi, H. R., & Reza, M. (2018). International Journal of Heat and Mass Transfer Natural convection heat transfer enhancement in new designs of plate-fin based heat sinks. *International Journal of Heat and Mass Transfer, 125*, 640–647. https://doi.org/10.1016/j.ijheatmasstransfer.2018.04.122

Hameed, V. M., & Khaleel, M. A. (2019). A study on the geometry and shape effects on different aluminum fin types of a vertical cylindrical heat sink. *Heat and Mass Transfer, 56*(4), 1317–1328.

Herlambang, Y. D., et al. (2022). Experimental and Simulation Investigation on Savonius Turbine: Influence of Inlet-Outlet Ratio Using a Modified Blade Shaped to Improve Performance. *Evergreen, 9*(2), 457–464. https://doi.org/10.5109/4794172

Hooman, K. (2018). Theoretical analysis of free convection in a partially foam-filled enclosure. *Heat and Mass Transfer, 55*, 1937–1946.

Huang, R., Sheu, W., & Wang, C. (2008). Orientation effect on natural convective performance of square pin fin heat sinks. *International Journal of Heat and Mass Transfer, 51*, 2368–2376. https://doi.org/10.1016/j.ijheatmasstransfer.2007.08.014

Jaffar, H. A., Ismaeel, A. A., & Shuraiji, A. L. (2022). Review of Hybrid Photovoltaic-Air Updraft Solar Application: Present and Proposed state Models. *Evergreen, 9*(4), 1181–1202. https://doi.org/10.5109/6625729

Kanargi, B., Lee, P. S., & Yap, C. (2018). International Journal of Heat and Mass Transfer A numerical and experimental investigation of heat transfer and fluid flow characteristics of an air-cooled oblique-finned heat sink. *International Journal of Heat and Mass Transfer, 116*, 393–416.

Kanargi, O. B., Lee, P. S., & Yap, C. (2017). A numerical and experimental investigation of heat transfer and fluid flow characteristics of a cross-connected alternating converging–diverging channel heat sink. *International Journal of Heat and Mass Transfer, 106*, 449–464. https://doi.org/10.1016/j.ijheatmasstransfer.2016.08.057

Khattak, Z., & Ali, H. M. (2019). Air cooled heat sink geometries subjected to forced flow: A critical review. *International Journal of Heat and Mass Transfer, 130*, 141–161. https://doi.org/10.1016/j.ijheatmasstransfer.2018.08.048

Kumar, N., Singh, M. K., Yadav, V. S., Singh, V., & Maheswari, A. (2023). A comparative analysis of ribs and cans type solar air heater. *Evergreen, 10*(3), 1449–1459. https://doi.org/10.5109/7151694

Lampio, K., & Karvinen, R. (2018). A new method to optimize natural convection heat sinks. *Heat Mass Transf. und Stoffuebertragung, 54*(8), 2571–2580. https://doi.org/10.1007/s00231-017-2106-4

Li, H. Y., & Chao, S. M. (2009). Measurement of performance of plate-fin heat sinks with cross flow cooling. *International Journal of Heat and Mass Transfer, 52*(13–14), 2949–2955. https://doi.org/10.1016/j.ijheatmasstransfer.2009.02.025

Lin, S. C., Chuang, F. S., & Chou, C. A. (2005). Experimental study of the heat sink assembly with oblique straight fins. *Experimental*

Thermal and Fluid Science, 29(5), 591–600. https://doi.org/10.1016/j.expthermflusci.2004.08.003

Luo, J. W., Chen, L., Xia, Y., Zheng, X., & Tao, W. Q. (2024). Three-dimensional multi-scale topology optimization of porous heat sink with predetermined unit cells for natural convection heat transfer. *International Journal of Heat and Mass Transfer, 225*(February), 125398. https://doi.org/10.1016/j.ijheatmasstransfer.2024.125398

Maheswari, A., & Prajapati, Y. K. (2022). Thermal performance enhancement and optimization of double-layer microchannel heat sink with intermediate perforated rectangular fins. *International Journal of Thermal Sciences, 185*(May), 2023. https://doi.org/10.1016/j.ijthermalsci.2022.108043

Moradikazerouni, A., et al. (2019). Comparison of the effect of five different entrance channel shapes of a micro-channel heat sink in forced convection with application to cooling a supercomputer circuit board. *Applied Thermal Engineering, 150*, 1078–1089.

Muneeshwaran, M., Tsai, M., & Wang, C. (2023). Heat transfer augmentation of natural convection heat sink through notched fin design. *International Communications in Heat and Mass Transfer, 142*, 106676. https://doi.org/10.1016/j.icheatmasstransfer.2023.106676

Naqiuddin, N. H., et al. (2018). Numerical investigation for optimizing segmented micro-channel heat sink by Taguchi-Grey method. *Applied Energy, 222*(March), 437–450. https://doi.org/10.1016/j.apenergy.2018.03.186

Okab, A. K., Hasan, H. M., Hamzah, M., Egab, K., & Al-manea, A. (2022). Analysis of heat transfer and fluid flow in a microchannel heat sink with sidewall dimples and fillet profile. *International Journal of Thermofluids, 15*(April), 100192.

Ranjbarzadeh, R., Kazerouni, A. M., Bakhtiari, R., Asadi, A., & Afrand, M. (2018). An experimental study on stability and thermal conductivity of water/silica nanofluid: Eco-friendly production of nanoparticles. *Journal of Cleaner Production*. https://doi.org/10.1016/j.jclepro.2018.09.205

Singh Yadav, V., Singh, V., Kumar, M., & Kumar, N. (2022). Optimization and Validation of Solar Pump Performance by MATLAB Simulink and RSM. 九州大学グリーンテクノロジー研究教育センター バージョン: 権利関係: *Evergreen. Joint Journal of Novel Carbon Resource Sciences and Green Asia Strategy*, *9*(4), 1110–1125, 2022, https://doi.org/10.5109/6625723.

Singh, P., & Patil, A. K. (2015). Experimental investigation of heat transfer enhancement through embossed fin heat sink under natural convection. *Experimental Thermal and Fluid Science, 61*, 24–33. https://doi.org/10.1016/j.expthermflusci.2014.10.011

Singh, V., & Yadav, V. S. (2022). Optimizing the performance of solar panel cooling apparatus by application of response surface methodology. *Proceedings of the Institution of Mechanical Engineers, Part c: Journal of Mechanical Engineering Science*. https://doi.org/10.1177/09544062221101828

Singh, V., Yadav, V. S., Kumar, N., Kumar, M., & Singh, M. K. (2023b). Optimum design and analysis of solar pump with the help of genetic algorithm, a MATLAB tool, and RSM tool at minimum cost. *Environmental Progress and Sustainable Energy*. https://doi.org/10.1002/ep.14308

Singh, V., Yadav, V. S., Trivedi, V., & Singh, M. K. (2023a). Performance optimization of solar pump operating by PV module. *Environmental Progress and Sustainable Energy*. https://doi.org/10.1002/ep.14293

Singh, V., Yadav, V. S., Yadav, V. K., Kumar, N., Kumar, M., Maheswari, A., & PrakashUpadhyaya, O. M. (2021). Experimental and computational investigation of flow fields using accelerated erosion test ring (AETR). *Journal of Engineering Research*. https://doi.org/10.36909/JER.ICCEMME.15599

Sohel Murshed, S. M., & Nieto de Castro, C. A. (2017). A critical review of traditional and emerging techniques and fluids for electronics cooling. *Renewable and Sustainable Energy Reviews, 78*(February), 821–833. https://doi.org/10.1016/j.rser.2017.04.112

Subasi, A., Sahin, B., & Kaymaz, I. (2016). Multi-objective optimization of a honeycomb heat sink using Response Surface Method. *International Journal of Heat and Mass Transfer, 101*, 295–302. https://doi.org/10.1016/j.ijheatmasstransfer.2016.05.012

Tari, I., & Mehrtash, M. (2013). International journal of heat and mass transfer natural convection heat transfer from inclined plate-fin heat sinks. *International Journal of Heat and Mass Transfer, 56*(1–2), 574–593. https://doi.org/10.1016/j.ijheatmasstransfer.2012.08.050

Tejas Sonawane, M., Prafulla Patil, M., Chavhan, M. A., Dusane, B. M., & Management, N. (2016). A review on heat transfer enhancement by passive methods. *International Research Journal of Engineering and Technology 3*(9), 1567–1574. [Online]. Available: www.irjet.net.

Verma, K., Prakash, O., Paikra, A. S., & Tiwari, P. (2023). Photovoltaic Panel Integration Using Phase Change Material (PCM): Review. *Evergreen, 10*(1), 444–453. https://doi.org/10.5109/6782147

Waila, V. C., Sharma, A., & Yusuf, M. (2022). Optimizing the performance of solar PV water pump by using response surface methodology. *Evergreen, 9*(4), 1151–1159. https://doi.org/10.5109/6625726

Xiang, J., Deng, L., Zhou, C., Zhao, H., Huang, J., & Tao, S. (2022). Heat Transfer Performance and Structural Optimization of a Novel Micro-channel Heat Sink. *Chinese Journal of Mechanical Engineering (English Edition)*. https://doi.org/10.1186/s10033-022-00704-5

Xie, G., Chen, Z., Sunden, B., & Zhang, W. (2013). Comparative study of the flow and thermal performance of liquid-cooling parallel-flow and counter-flow double-layer wavy microchannel heat sinks. *Numerical Heat Transfer, Part a: Applications, 64*(1), 30–55. https://doi.org/10.1080/10407782.2013.773811

Yang, A., Chen, L., Xie, Z., Feng, H., & Sun, F. (2019). Constructal operation cost minimization for in-line cylindrical pin-fin heat sinks. *International Journal of Heat and Mass Transfer, 129*, 562–568. https://doi.org/10.1016/j.ijheatmasstransfer.2018.09.129

Zhao, L., Xing, Y., & Liu, X. (2020). Experimental investigation on the thermal management performance of heat sink using low melting point alloy as phase change material. *Renewable Energy, 146*, 1578–1587. https://doi.org/10.1016/j.renene.2019.07.115